Characteristics and signatures of dipole vortices in ferroelectric nanodots: First-principles-based simulations and analytical expressions

S. Prosandeev[1,2] and L. Bellaiche[1]

[1]*Physics Department, University of Arkansas, Fayetteville, Arkansas 72701, USA*

[2]*Institute of Physics, Rostov State University, Rostov on Don 344090, Russia*

Characteristics and signatures of dipole vortex in ferroelectric nanodots are determined via the use of first-principles-based simulations and by analytical developments. For instance, the dependency of such vortex on size, shape, material, and temperature is provided. Moreover, peculiar features associated with such vortex, such as unique behaviors of the inhomogeneous and homogeneous strains and of the induced electric fields, are revealed. Finally, energetics of interacting vortices is also discussed.

　　　　　　　　　　PACS number(s): 77.84.Dy, 77.80.Bh, 77.22.Ej

I. INTRODUCTION

Recently, first-principles-based simulations predicted the existence of an unusual phenomena in nanodots of ferroelectrics, that is, the formation of a vortex structure for their electrical dipoles below a critical temperature.[1–3] Similar to magnetic nanostructures that also possess a vortex structure for their magnetic dipoles (which is usually referred to as the curling state),[4–6] the possibility of switching the chirality of the vortex in ferroelectric nanostructures opens exciting opportunities for designing "wunderbar" nanomemory devices.[2,7] Interestingly, while *ab initio* studies[2,7] suggested original ways to allow a practical control of the vortex chirality (namely, by using an *inhomogeneous* static electric field[7] or a time-dependent magnetic field[2]), dipole vortex in nanoferroelectrics remains to be *experimentally* found—to the best of our knowledge. One plausible reason for this lack of finding may be (in addition to the inherent difficulty in growing nanoferroelectrics) the current paucity of knowledge about the possible "signatures" of a dipole vortex. For instance, one may wonder how an electric field produced by a vortex differs from the one generated by a polarized sample. Similarly, it may be worthwhile to know if the strain associated with the vortex structure is dramatically different than the one associated with a spontaneous polarization. Other important and related issues that are poorly known (if not completely unknown) are the dependency of the vortex structure on the shape of the dot as well as on the material forming the dot, the energy landscape associated with vortices, or the energetics of interacting vortices.

The aim of this paper is to provide characteristics and signatures of dipole vortices in ferroelectric nanodots by performing first-principles-based computations as well as by deriving analytical expressions for electric fields generated by a vortex structure. This paper is organized as follows. Section II describes the *ab initio* method we used. In Sec. III, important atomistic, elastic, and energetic characteristics of vortex are revealed. Sections IV and V focus on the electric field produced by a vortex structure inside and outside a ferroelectric nanodot, respectively. Section VI discusses the energetics of interacting dipole vortices, while a summary is provided in Sec. VII. An Appendix is also offered for better understanding the origins of some formula given in Secs. V and VI.

II. EFFECTIVE HAMILTONIAN APPROACH

Here, we mostly study nanodots made of disordered $PbZr_{0.4}Ti_{0.6}O_3$ (PZT60), being Pb-O terminated at all surfaces. We also investigate nanodots made of $BaTiO_3$ (BT), being Ba-O terminated at all surfaces, for the sake of comparison with PZT60 nanodots. The total energy of such systems is written as

$$\mathcal{E}_{tot}(\mathbf{u}_i, \mathbf{v}_i, \eta_H) = \mathcal{E}_{Heff}(\mathbf{u}_i, \mathbf{v}_i, \eta_H) + \beta \sum_i \langle \mathbf{E}_{dep} \rangle \cdot Z^* \mathbf{u}_i, \quad (1)$$

where $\mathbf{u}_i$ is the local soft mode in the unit cell i of the dot, whose product with the effective charge Z^* yields the local electrical dipole in this cell, while η_H and $\mathbf{v}_i$ are the homogeneous strain tensor and inhomogeneous strain-related variables in unit cell i, respectively.[8]

$\mathcal{E}_{Heff}$ represents the intrinsic (effective Hamiltonian) energy of ferroelectric nanodots. Its analytical expression is the one of Ref. 8 for BT bulk and of Ref. 9 for PZT60 bulk (while its first-principles-derived parameters are those of Ref. 10 for BT and of Ref. 9 for PZT60), except for two main modifications. The first modification consists in adding energetic terms associated with the direct interaction between the vacuum surrounding the dot and both the surface dipoles and inhomogeneous strain near the surface.[1,11] The second modification consists in replacing the (reciprocal-space-based) matrix associated with long-range dipole-dipole interactions in the bulk[8] by the corresponding (real-space-based) matrix characterizing dipole-dipole interactions in the dot, implying that no supercell periodic boundary conditions are needed to simulate the dot. Such matrix is given in Refs. 3 and 12 and corresponds to ideal open-circuit (OC) conditions. Such electrical boundary conditions naturally lead to the existence of a maximum depolarizing field (denoted by $\langle \mathbf{E}_{dep} \rangle$ and determined from the atomistic approach of Ref. 3) inside the dot. The second term of Eq. (1) mimics a screening of $\langle \mathbf{E}_{dep} \rangle$ via the β parameter. More precisely, the residual depolarizing field resulting from the combination of the first and second terms of Eq. (1) has a magnitude equal to $(1-\beta)|\langle \mathbf{E}_{dep} \rangle|$. $\beta=0$ thus corresponds to ideal OC conditions, while an increase in β lowers the magnitude of the
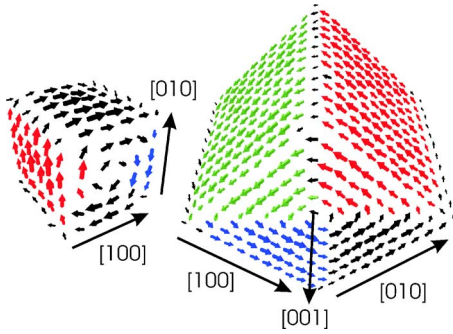
FIG. 1. (Color online) (001) Dipole vortex in a stress-free $6 \times 6 \times 6$ (left) and $12 \times 12 \times 12$ (right) nanodots of PZT60 at 1 K under open-circuit conditions.

resulting depolarizing field, and $\beta=1$ corresponds to ideal short-circuit (SC) conditions for which the depolarizing field has vanished.

Technically, we perform 2×10^4 Monte Carlo sweeps to, first, equilibrate the system, and then, another 2×10^4 Monte Carlo sweeps to obtain the statistical averages for a given temperature. The strain tensor is allowed to fully relax, which implies that we mimic *stress-free* nanodots. Typically, the temperature is decreased in small steps down to 1 K in order to get the equilibrium ground-state properties.

III. CHARACTERIZATION OF A DIPOLE VORTEX

A. Dipole patterns

As was indicated in Refs. [1–3] and [7], stress-free ferroelectric nanodots under open-circuit-like conditions exhibit a ground-state structure consisting of a vortex for their local dipoles. Such striking ground state is shown in Fig. [1] for 6 $\times 6 \times 6$ and $12 \times 12 \times 12$ PZT60 dots, i.e., for two cubic nanodots of lateral size around 24 and 48 Å, respectively, as predicted by our effective Hamiltonian method. Figure [1] indicates that no spontaneous polarization exists for the ferroelectric dots exhibiting the vortex pattern. This contrasts with magnetic dots for which a dipole vortex also exists but with a core possessing a magnetization.[13] The reason behind such difference lies in a stronger exchange interaction and weaker cubic anisotropy in magnets in comparison with ferroelectrics.[1–3,7]

Figure [1] also indicates that increasing the size in ferroelectric dots results in having a larger proportion of dipoles aligned, or close to be aligned, along four possible $\langle 001 \rangle$ directions with respect to those significantly rotating away from $\langle 001 \rangle$ in this vortex pattern. [Note that $\langle 001 \rangle$ directions are the possible directions for the polarization in the (tetragonal) ground state of *bulk* PZT60.[14]] As a result, one can also think of the vortex structure of large ferroelectric dots as being made of four different domains, each having dipoles aligned along a specific $\langle 001 \rangle$ direction, with 90° domain walls between the domains—which is a solution that was actually proposed many years ago by Kittel.[15]

We also compare in Fig. [2] the dipole patterns obtained in a $12 \times 12 \times 12$ PZT60 dot and a $12 \times 12 \times 12$ BT dot, mainly to know if the fact that PZT60 and BT bulks have different
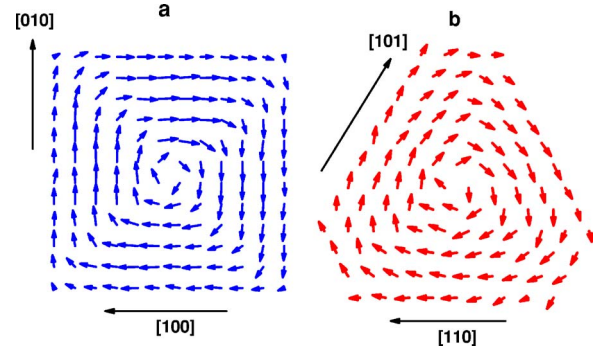

FIG. 2. (Color online) Cross section of a dipole vortex in a stress-free $12 \times 12 \times 12$ dot (under open-circuit conditions) made of (a) PZT60 in a {001} plane and (b) $BaTiO_3$ in a {111} plane at 1 K.

ground states with dipoles lying along different directions (BT bulk has a rhombohedral ground state with dipoles pointing along a $\langle 111 \rangle$ direction) affects the vortex structure in the corresponding nanodots. Interestingly, Fig. [2] reveals that the direction of the vortex in the dots is a possible direction of the polarization in the bulk, namely, the direction of the vortex in the PZT60 nanodots is along a $\langle 001 \rangle$ direction while it is along a $\langle 111 \rangle$ direction in the BT dot. This implies that the direction of the dipoles in the BT nanodot lies in a {111} plane. As a result, dipoles in the ground state of the BT nanodot are *not* parallel to any possible direction of the dipoles in the ground state of BT bulk [these dipoles are mostly directed along $\langle 011 \rangle$ directions in the BT dot, as indicated in Fig. [2(b)]]. Another striking difference between BT bulks and nanodots consists in the *number* of phase transitions: the bulk is known to experience three phase transitions (namely, paraelectric cubic-to-ferroelectric tetragonal, ferroelectric tetragonal to ferroelectric orthorhombic, and ferroelectric orthorhombic-to-ferroelectric rhombohedral[8]) when decreasing the temperature, while we numerically found that there is a single transition in the investigated BT nanodot. This single transition is from a paraelectric state to a state exhibiting the vortex structure shown in Fig. [2(b)].

The dipole vortex can also exist in nanodots of different shapes. For instance, Fig. [3] shows such vortex for PZT60 dots having rectangular ($16 \times 16 \times 8$ and $12 \times 24 \times 12$), spherical ($16 \times 16 \times 16$), and pyramidal ($16 \times 16 \times 8$) shapes. The rectangular and pyramidal dots have vortices directed along the shortest (c) axis, while the vortex in the spherical dot can be oriented along any $\langle 001 \rangle$ direction (because of symmetry considerations). Interestingly, the dipoles in the rectangular dots mostly all lie along four possible $\langle 001 \rangle$ directions, while larger deviation of some dipoles from $\langle 001 \rangle$ can be seen in a spherical dot. One can also see that the bigger ($12 \times 24 \times 12$) rectangular dot has two vortices with opposite directions, which contrasts with the case of the shorter ($16 \times 16 \times 8$) rectangular dot showing only one vortex. In the bigger rectangular dot, the dipole flux between the vortices is uniform, as in elongated cylinders[2] and in arrays of ferroelectric dots embedded in less polarizable media.[16] Short-range and elastic interactions are responsible for such antiphase orientation, since (as we will see in Sec. VI) the long-range dipole-dipole interaction favors a parallel orientation of the vortices.
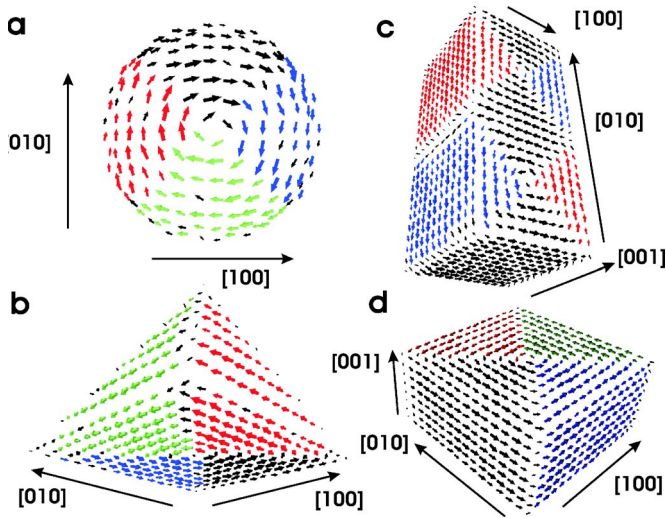
FIG. 3. (Color online) The dipole pattern obtained in our Monte Carlo computation at 1 K for stress-free spherical $16 \times 16 \times 16$ (a), pyramidal $16 \times 16 \times 8$ (b), rectangular $12 \times 12 \times 24$ (c), and rectangular $16 \times 16 \times 8$ (d) nanodots made of PZT60 and under open-circuit conditions.

B. Strain

Figure 4 shows the η_1, η_2, η_3, and η_6 components of the *total* strain tensor (that is, containing homogeneous and inhomogeneous parts) in a $12 \times 12 \times 12$ nanodot of PZT60 at a low temperature. The other components, in Voigt notation, are negligible and thus not shown. One can clearly see that the component of the strain tensor associated with the direction of the vortex (i.e., η_3) is rather homogeneous and small, while the other displayed components exhibit significant changes inside the dot because of the coupling between the dipoles making the vortex and the strain.[8] For instance, we numerically found that η_1 is large in the regions of the dot
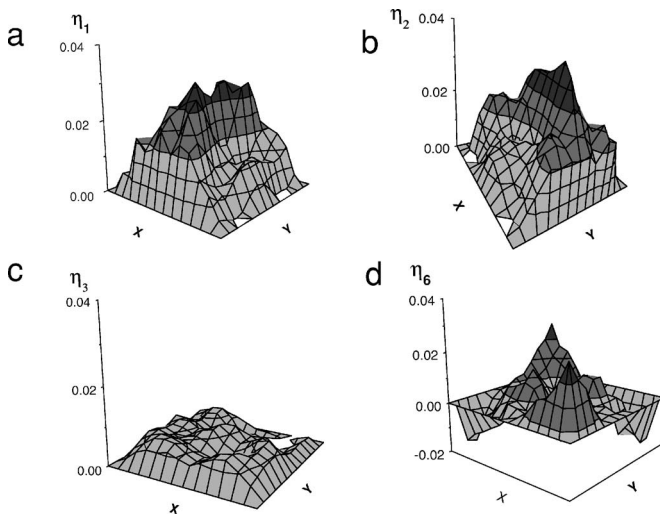

FIG. 4. Total strain (in Voigt notation) in the middle (001) atomic plane in a stress-free cubic $12 \times 12 \times 12$ nanodot made of PZT60 (under open-circuit conditions and having the toroidal moment oriented along z), as computed by the Monte Carlo method at 1 K: (a) η_1, (b) η_2, (c) η_3, and (d) η_6.
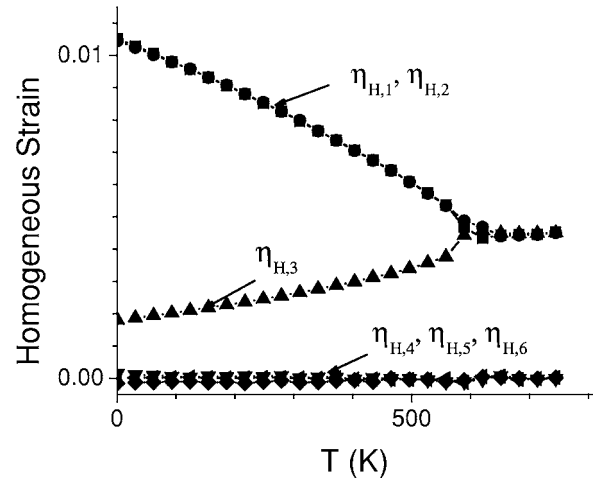

FIG. 5. Homogeneous strain versus temperature in a stress-free cubic $12 \times 12 \times 12$ nanodot made of PZT60 and under open-circuit conditions. The temperature has been rescaled in order to match the experimental Curie temperature of bulk PZT.

having dipoles oriented along x and $-x$, while it is much smaller in the domains having the local modes in the y and $-y$ directions. Interestingly, such coupling implies that the nanodot having the dipole vortex directed in the z direction is more elongated in the directions perpendicular to z than along the z direction. Such feature can be guessed from Fig. 4 and is clearly further revealed by Fig. 5 that shows the $\{\eta_H\}$ *homogeneous* strain versus temperature. One can see that $\eta_{H,3}$ is smaller than $\eta_{H,2} = \eta_{H,1}$, below the temperature at which the vortex pattern forms (which is around 600 K). In other words, the tetragonal axial ratio c/a is lower than 1 for vortex in dots, which contrasts with the axial ratio in tetragonal systems exhibiting either a spontaneous polarization[14] or the condensation of antiferrodistortive motions.[17] Such unique strain feature may be put in use to experimentally identify the vortex structure in ferroelectrics.

Figure 4 also indicates that the largest magnitudes of the η_1 and η_2 total strains are achieved in the area close to the center of the vortex (because of the elastic elongation of *all* four domains constituting the vortex), and that these magnitudes are considerably larger than the corresponding homogeneous strain. Such large enhancement of the local strain may lead to the appearance of cracks in the center of the dot as proposed by Tikadzumi.[18] We have found that one possibility to avoid the large strain at the origin of the dipole vortex is to cut a hole in the center of the dot, that is, to make a ring. Figure 6 shows the result of our computation for the η_1 component of the total strain tensor for a cubic nanodot $12 \times 12 \times 12$ with a cylindrical hole of $6 \times 6 \times 12$ dimension in the middle. One can see that this strain in such a nanoring adopts a much smaller maximum value, and has a much weaker deviation with respect to the homogeneous strain (equal to 0.01), than the corresponding strain component of the cubic nanodot. [It is interesting to realize that making holes in the middle of nanodots made of magnets has also been mentioned in the literature.[19] However, in that case, it is to create a perfect vortex structure (rather than to decrease the local strain magnitude) since the center of a magnetic
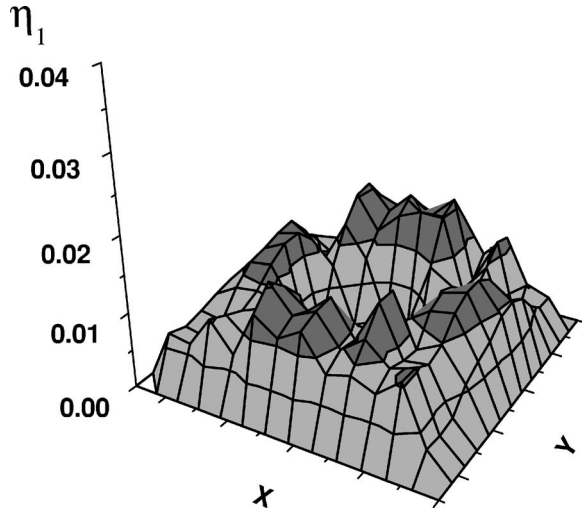
FIG. 6. The η_1 component of the total strain (in Voigt notation) in the middle (001) atomic plane in a stress-free cubic $12 \times 12 \times 12$ PZT60 nanodot (under open-circuit conditions) with a $6 \times 6 \times 6$ cylindrical hole in the middle, as computed by the Monte Carlo method at 1 K.
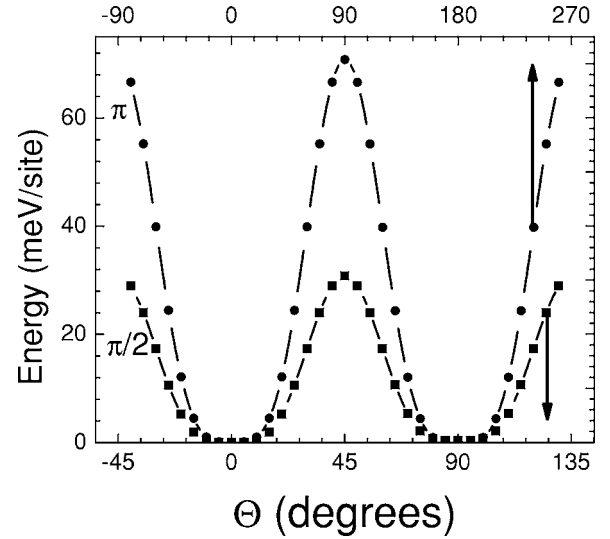

FIG. 7. Total energy of a stress-free $12 \times 12 \times 12$ PZT60 nanodot at 1 K (under open-circuit conditions) versus the Θ angle (see text).

nanodot has a magnetized core that works against the vortex structure, especially in small nanodots.]

Obviously, large local strain "only" occurs if the electrostriction coefficients are large, or equivalently, if the coupling between dipoles and strain is significant. Inversely, one may wonder if neglecting such coupling can lead to the disappearance of the vortex structure. In order to check this possibility, we switched off the electrostriction interactions during the simulations, but still obtained the dipole vortex structure albeit with a weaker magnitude of the dipoles. This indicates that the coupling between strain and dipoles favors the vortex structure, but is not the main cause of the existence of such vortex. Such cause originates from depolarizing field effects.[1–3,7]

C. Toroidal moment and potential wells

The vortex patterns in ferroelectric nanoparticles can be characterized by a **G** toroidal moment,[2,20]

$$\mathbf{G} = \frac{1}{2N} \sum \mathbf{r}_i \times \mathbf{p}_i, \qquad (2)$$

where $\mathbf{r}_i$ and $\mathbf{p}_i$ are the vector locating the cell i and the dipole moment of this cell, respectively. N is the number of B sites. Interestingly, **G** in ferroelectric dots is an axial vector, and thus does neither change under the inversion of space nor is altered under time inversion symmetry. On the other hand, because of the difference in symmetry between electric dipoles versus magnetic dipoles, the toroidal moment of magnetic dots is a polar vector and thus breaks both the space and time inversion symmetry.[20]

For the vortices shown in Fig. 1, the direction of **G** in the PZT60 dots coincides with one of the ⟨001⟩ axes. Due to the cubic symmetry of these dots, the toroidal moment can also be parallel or antiparallel to any other ⟨001⟩ direction with

equal probability. In other words, the ground state is six times degenerated. To have an idea about the magnitude of the potential barriers between these six states, we first performed several Monte Carlo (MC) computations for a $12 \times 12 \times 12$ stress-free nanodot of PZT60 under open-circuit electrical boundary conditions. Such computations provide us with (at least) three ground states (to be denoted by states 1, 2, and 3) associated with different directions for the toroidal moment. More precisely, the angle made by the toroidal moments of states 1 and 2 is 90°, while the toroidal moments of states 1 and 3 are exactly opposite in direction (i.e., their angle is 180°). We then construct two new sets of configurations, to be denoted by states 4 and 5, for which

$$\mathbf{u}_i^{(4)} = \cos^2(\theta)\mathbf{u}_i^{(1)} + \sin^2(\theta)\mathbf{u}_i^{(2)} \qquad (3)$$

and $\mathbf{u}_i^{(5)} = \cos^2(\theta/2)\mathbf{u}_i^{(1)} + \sin^2(\theta/2)\mathbf{u}_i^{(3)}, \qquad (4)$

where $\mathbf{u}_i^{(1)}$, $\mathbf{u}_i^{(2)}$, $\mathbf{u}_i^{(3)}$, $\mathbf{u}_i^{(4)}$, and $\mathbf{u}_i^{(5)}$ are the local modes at the B-sites i in states 1, 2, 3, 4, and 5, respectively. Θ is an angle that is practically varied by small steps from zero to 90° (respectively, 180°) to sample all the states 4 (respectively, 5) continuously connecting state 1 and state 2 (respectively, state 3). Note that the toroidal moment of states 4 and 5 makes an angle of θ with respect to **G** of state 1. For each angle θ, we then perform MC simulations at small temperature, keeping the values of the local modes in state 4 (respectively, 5) as those given by Eq. (3) [respectively, Eq. (4)] but allowing the homogeneous and inhomogeneous strains to relax in order to minimize the total energy. Figure 7 shows this latter quantity at the end of the MC procedure, and reveals that (1) the potential wells are separated by relatively large barriers, and (2) the 180° barrier (that involves a paraelectric state located halfway between states 1 and 3) is higher than the 90° one (located halfway between states 1 and 2).
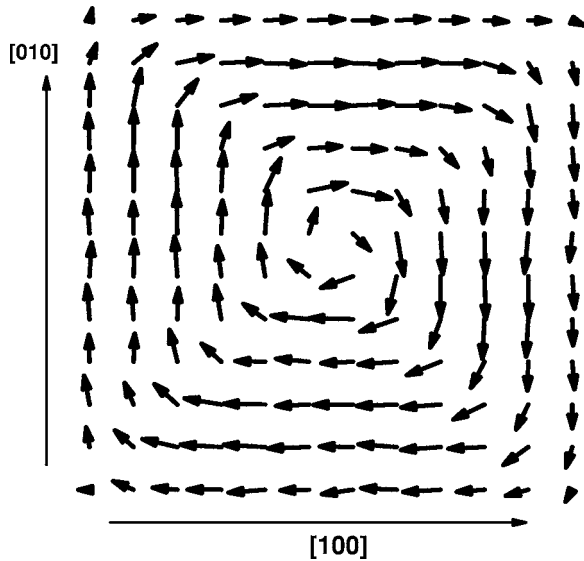
FIG. 8. Local field $\mathbf{E}_i$ (see text) in a {001} plane of a stress-free cubic PZT60 $12 \times 12 \times 12$ nanodot at 1 K and under open-circuit conditions.

IV. LOCAL FIELD INSIDE CUBIC NANODOTS

The local electric field $\mathbf{E}_i$ produced at the i site by all the dipoles of the dot *but the one of site i* is shown in Fig. 8 for a $12 \times 12 \times 12$ PZT60 nanodot under open-circuit and stress-free boundary conditions. One can see that the local field $\mathbf{E}_i$ inside the dot is highly anisotropic and adopts a vortex pattern. Interestingly, we found that this microscopic field $\mathbf{E}_i$ is, on average, close to $(1/3\varepsilon_0)\,\mathbf{P}_i$, where ε_0 is the dielectric permittivity of vacuum and $\mathbf{P}_i$ is the local polarization at the site i. (Practically, $\mathbf{P}_i$ is calculated as $Z^*\mathbf{u}_i/a^3$, where $\mathbf{u}_i$ is the local mode at that site, Z^* is the dynamical charge, and a is the 0 K cubic lattice constant of the primitive unit cell.) For instance, the electrostatic energy computed from $-\Sigma_i\mathbf{P}_i\cdot\mathbf{E}_i$, with $\mathbf{E}_i=(1/3\varepsilon_0)\,\mathbf{P}_i$, differs by less than 10% from the value directly obtained in our numerical simulations. The local field $\mathbf{E}_i$ is thus rather strong at any site i. This strength, as well as the overall vortex pattern made by the $\mathbf{E}_i$ of all the different sites, can be thought of as binding the dipole of site i to the vortex dipole pattern. In other words, this field draws the ions from their centrosymmetrical positions to adopt positions associated with a vortex structure. Moreover, the vortex pattern of $\mathbf{E}_i$ depicted in Fig. 8 implies that the *average* electric field produced by the dipole vortices inside the nanodots *vanishes*, which explains the appearance of the dipole vortices in nanodots instead of a uniform polarization (that would lead to an energetically costly depolarizing field).

Furthermore, it was previously shown[3] that the dipole vortices can occur even if a large amount of the maximum depolarizing field is screened by, e.g., external short-circuited metallic plates. Let β be the parameter indicating the amount of screening of the depolarizing field, see Sec. II. In other words, β can range between 0 and 1, with $\beta=0$ corresponding to no screening at all (ideal open-circuit conditions), while $\beta=1$ corresponds to a full screening (ideal short-circuit conditions). Figure 9 shows the total energy of a
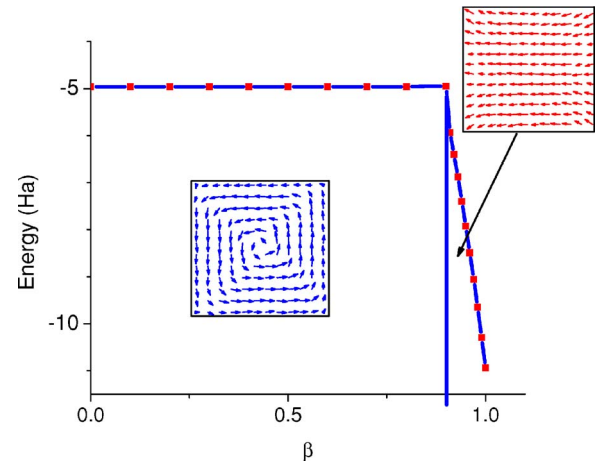

FIG. 9. (Color online) Dependence of the total energy of a stress-free cubic PZT60 $12 \times 12 \times 12$ nanodot on the β screening parameter at 1 K. The insets show the two different kinds of dipole pattern existing for the possible β values.

PZT60 $12 \times 12 \times 12$ cubic nanodot as a function of β and obtained at 1 K. As discovered in Ref. 3, two kinds of dipole pattern exist: for large β, the dot is polarized, while β smaller than $\simeq 0.9$ gives rise to the vortex structure. These two patterns are schematized in the insets of Fig. 9. Interestingly, decreasing β from its ideal short-circuit value of 1 first results in decreasing the total energy of the polarized dot in response to the increasing-in-magnitude depolarizing field (with the dipoles decreasing in magnitude when β decreases). Then, as soon as the vortex structure is created, the average electric field inside the vortex pattern is null, and thus no depolarizing field exists. As a result, the total energy (as well as the magnitude of the dipoles) does not depend on β anymore.

V. ELECTRIC FIELD PRODUCED BY A LATTICE DIPOLE VORTEX OUTSIDE THE DOT

Let us now discuss the electric field produced by the dipole vortex *outside* the dot. For that, we first consider the electric field acting at a position $\mathbf{R}$ and produced by dipoles $\mathbf{p}_i$ located at $\mathbf{r}_i$ with respect to a selected point (to be chosen as the origin):

$$\mathbf{E} = -\frac{1}{4\pi\varepsilon_0\varepsilon^*}\sum_i \frac{R_i^2\mathbf{p}_i - 3(\mathbf{p}_i\mathbf{R}_i)\mathbf{R}_i}{R_i^5}. \qquad (5)$$

Here $(\mathbf{p}_i\mathbf{R}_i)$ is the dot product of $\mathbf{p}_i$ and $\mathbf{R}_i$, $\mathbf{R}_i=\mathbf{R}-\mathbf{r}_i$, R_i is the magnitude of the vector $\mathbf{R}_i$, ε_0 is the vacuum permittivity, and $\varepsilon^*=(\varepsilon_1+2)/3$ [with ε_1 being the high-frequency (electronic) dielectric permittivity of the dot], which technically corresponds to dots of spherical shape surrounded by vacuum (see Appendix).

The expansion of this field with respect to $\mathbf{r}_i$, for $|\mathbf{r}_i| \ll |\mathbf{R}|$, gives $\mathbf{E}=\Sigma_k\mathbf{E}^{\{k\}}$, where the upper index k $(=1,2,3,\ldots)$ represents the order of $\mathbf{r}_i$ appearing in $\mathbf{E}^{\{k\}}$. For instance, the first-order term is given by

TABLE I. The independent components of the M tensor (in e Å^4) and the toroidal moment (in e Å^2 and oriented along the z axis) for two stress-free cubic nanodots of PZT60 at 1 K and under open-circuit conditions, as obtained in our Monte Carlo computations.

Dot's size	M_{1222}	M_{1233}	M_{1211}	M_{3333}	M_{3311}	$M_{1222}-3M_{1211}$	G_z
$6\times6\times6$	791	459	293	−48	−25	−88	−10.6
$12\times12\times12$	8394	4788	2863	−232	−120	−195	−27.0

$$\mathbf{E}^{(1)} = -\frac{3}{4\pi\varepsilon_0\varepsilon^*R^5}\sum_i\left\{[(\mathbf{r}_i\mathbf{R})\mathbf{p}_i+(\mathbf{p}_i\mathbf{R})\mathbf{r}_i]-(\mathbf{p}_i\mathbf{r}_i)\mathbf{R}\right.$$
$$\left.+5\frac{(\mathbf{p}_i\mathbf{R})(\mathbf{r}_i\mathbf{R})\mathbf{R}}{R^2}\right\}. \tag{6}$$

In case of a symmetrical vortex (such as the ones displayed in Fig. 1) possessing the rotation by 90° (about the axis along which the toroidal moment lies) as one of its symmetry elements, this first-order contribution to the electric field is exactly zero. If such symmetry element is absent, Eq. (6) indicates that magnitude of the electric field decreases with the distance as $1/R^4$.

Interestingly, the first nonvanishing contribution to the electric field produced by a symmetrical vortex appears only in the third order. It is straightforward to prove that the expression of $\mathbf{E}^{\{3\}}$ can be written as

$$E_\kappa^{(3)} = \frac{N}{4\pi\varepsilon_0\varepsilon^*R^6}\left[\frac{15}{2}\sum_{\alpha\beta}(M_{\kappa\beta\alpha\alpha}+M_{\beta\kappa\alpha\alpha})n_\beta\right.$$
$$+15\sum_{\alpha\gamma}M_{\gamma\gamma\alpha\kappa}n_\alpha+\frac{15}{2}\sum_{\alpha\beta}M_{\beta\beta\alpha\alpha}n_\kappa$$
$$-\frac{105}{2}\sum_{\alpha\beta\gamma}M_{\gamma\gamma\alpha\beta}n_\alpha n_\beta n_\kappa-\frac{35}{2}\sum_{\alpha\beta\gamma}n_\alpha n_\beta n_\gamma(M_{\kappa\alpha\beta\gamma}$$
$$+3M_{\gamma\alpha\beta\kappa})-\frac{105}{2}\sum_{\alpha\beta\gamma}M_{\gamma\beta\alpha\alpha}n_\beta n_\gamma n_\kappa$$
$$+\frac{315}{2}\sum_{\alpha\beta\gamma\lambda}M_{\lambda\alpha\beta\gamma}n_\alpha n_\beta n_\gamma n_\lambda n_\kappa\right], \tag{7}$$

where N is the number of B sites in the dot; κ, α, β, γ, and λ denote Cartesian components ($=x,y,z$); $n_\alpha=R_\alpha/R$ with R_α being the projection of $\mathbf{R}$ along the α axis, and where the M fourth-rank tensor is given by

$$M_{\kappa\alpha\beta\gamma} = \frac{1}{N}\sum_i p_{i\kappa}r_{i\alpha}r_{i\beta}r_{i\gamma}. \tag{8}$$

Here, we will consider the case when the toroidal moment is along the z axis, with the symmetry of the dipole pattern corresponding to the 4, $\bar{4}$, or $4/m$ point group. In that case, the M tensor has the following eight nonzero independent components:[21] $M_{1111}=M_{2222}$, $M_{1222}=-M_{2111}$, $M_{1122}=M_{2211}$, $M_{1233}=-M_{2133}$, $M_{1133}=M_{2233}$, $M_{1211}=-M_{2122}$, M_{3333}, and $M_{3311}=M_{3322}$. It is important to realize that Eq. (8) implies that the M tensor is invariant by permutation of its last three indices. As a result, one should also take into account (in the

equalities above) all other components resulting from the permutation of the last three indices.

Dipole vortices can also possess additional symmetry, beyond the symmetry elements of the considered point groups. For instance, the operation consisting in, first, applying a mirror element located in a ZX plane and, then, inverting the direction of each dipole moment leaves the vortex structures shown in Fig. 1 unchanged. We analytically and numerically found that, owing to this additional (combined) symmetry, the following M tensor components vanish: $M_{1111}=M_{1122}=M_{1133}=0$. As a result, there are only five independent components of M for the considered vortices.

These components of the M tensor are given in Table I for stress-free $6\times6\times6$ and $12\times12\times12$ nanodots of PZT60 under open-circuit conditions at 1 K, as obtained by our Monte Carlo computations. For the sake of comparison, Table I also reports the toroidal moments in these dots. First, one can notice that the M_{3333} and M_{3311} components are much smaller than the other components, which results from the small values of the z component of the local modes in the corresponding vortex. Second, the M_{1222}, M_{1233}, and M_{1211} components all increase $\simeq$ four times faster than the toroidal moment when increasing the size of the nanodot, which is related to the fact that the M tensor involves the third order in $\mathbf{r}_i$ [see Eq. (8)] while the toroidal moment involves the first order in $\mathbf{r}_i$ [see Eq. (2)].

Figure 10 presents the predicted temperature dependency of the M_{1222} and M_{1211} components for a $12\times12\times12$ stress-
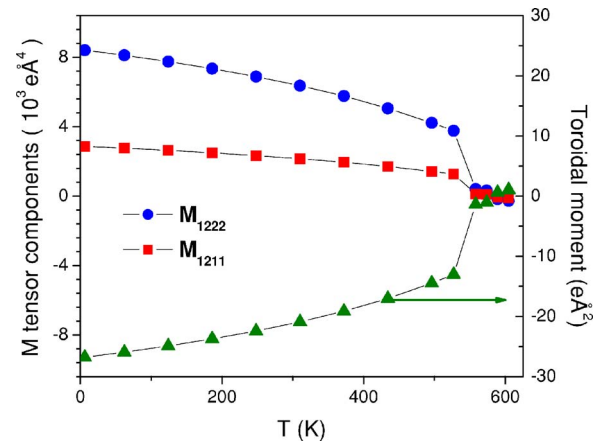

FIG. 10. (Color online) The temperature dependency of the M_{1222} and M_{1211} components of the M tensor (see text) together with the toroidal moment in a $12\times12\times12$ stress-free dot of PZT60 under open-circuit conditions, as obtained in our Monte Carlo computations. The temperature has been rescaled in order to match the experimental Curie temperature of bulk PZT.

free nanodot of PZT60 under open-circuit conditions. The behavior of the toroidal moment as a function of temperature is also shown in this figure. The temperature dependency of the components of the M tensor is similar to that of the toroidal moment: the M tensor components and the toroidal moment both sharply grow in magnitude below a critical temperature, and the ratio between the components of the M tensor and the toroidal moment is practically independent of temperature below the critical temperature.

Moreover, to better appreciate the characteristics of a field produced by a dipole vortex (such as the ones shown in Fig. 1), we found convenient to introduce the tangential $E_\varphi^{(3)}$ and radial $E_\rho^{(3)}$ components of the field (in the cylindrical coordinate system) defined as

$$E_\varphi^{(3)} = -\sin\varphi E_x^{(3)} + \cos\varphi E_y^{(3)},$$

$$E_\rho^{(3)} = \cos\varphi E_x^{(3)} + \sin\varphi E_y^{(3)}, \quad (9)$$

where φ is the polar angle (in cylindrical coordinates) of the **R** vector at which the field is acting. Note that we numerically found that the z component of the field produced by the dipole vortex in PZT60 is approximately zero, due to the symmetry of the vortex and due to the fact that the z component of the dipole moments is very weak. The analytical expressions of $E_\varphi^{(3)}$ and $E_r^{(3)}$ can be derived from Eq. (7) as follows:

$$E_\varphi^{(3)} = \frac{35N}{8\pi\varepsilon_0\varepsilon^* R^6}(M_{1222} - 3M_{1211})n_\rho^3\cos 4\varphi,$$

$$E_\rho^{(3)} = \frac{35N}{8\pi\varepsilon_0\varepsilon^* R^6}(M_{1222} - 3M_{1211})n_\rho^3\sin 4\varphi, \quad (10)$$

where $n_\rho = \sqrt{n_x^2 + n_y^2}$.

Figure 11 schematically shows the electric field produced by a dipole vortex in an XY plane at some fixed distance from the center of the XY cross section of the dot. (Note that the displayed pattern of this field does not qualitatively depend on the chosen radius nor on the chosen XY plane.) One can see from this figure and Eqs. (10) that this field oscillates (when varying φ), and thus leads to a vanishing value when averaging it over φ. The tangential component of the field vanishes at the angles $\varphi = \pi/8 + n\pi/4$, where $n = 0, 1, \ldots, 8$, while the radial component adopts maximal magnitude at these angles. Inversely, the tangential component of the field is maximum (with this maximum magnitude being equal to the maximum amplitude of the radial component) when the radial component is annihilated. The peculiar field pattern schematized in Fig. 11 is a definite signature of the dipole vortex (and also of its chirality).

Notice that Eqs. (10) indicate that the radial and tangential components of the field neither depend on M_{1233} nor on M_{1222} or M_{1211}, *separately*, but are rather functions of the $M_{1222} - 3M_{1211}$ difference. Interestingly, Table I further reveals that such difference, and thus the maximum amplitude of the radial and tangential components of the field, increases by a similar ratio as the toroidal moment when increasing the size of the nanodot.

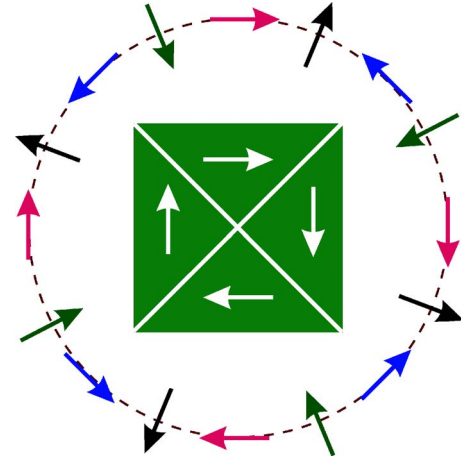Figure 12 displays the result of our Monte Carlo compu-

FIG. 11. (Color online) A schematic representation of the angular dependency of the electric field produced by a stress-free cubic ferroelectric nanodot under open-circuit conditions. The central square marks the XY cross section of the dot, while the arrows inside this dot show the direction of the dipoles in the different domains. The arrows outside the dot display the direction and relative magnitude of the electric field produced by the dipole vortex in an XY plane at some fixed distance from the center of the XY cross section of the dot.

tation for the electric field produced by a stress-free $12 \times 12 \times 12$ dot of PZT60 under open-circuit boundary conditions, as a function of the distance with respect to the center of the dot in the $z=0$ plane and for $\varphi=0$. One can see that, close to the dot boundary, the magnitude of this field reaches rather high values (about 10^8 V/m). Moreover, the dependence of this field on the distance is numerically found to be very close to $1/R^6$ for larger distance, consistent with Eqs. (10) (which were derived for large enough distances). Such dependency strongly differs with the corresponding one of $1/R^3$ associated with a polarization.
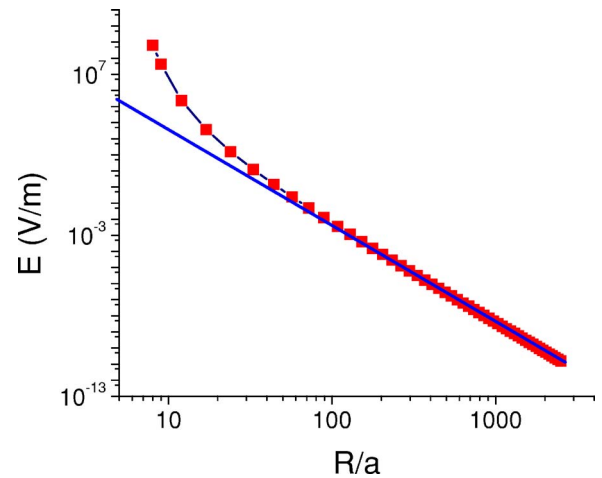

FIG. 12. (Color online) Dependency of the electric field magnitude produced by a $12 \times 12 \times 12$ stress-free dot of PZT60 (under open-circuit conditions) at 1 K on the distance with respect to the center of the dot (in units of the a lattice constant of the five-atom unit cell) as obtained in our Monte Carlo computations. The straight line shows the fit by A/R^6 (where A is a constant).

VI. INTERACTING DIPOLE VORTICES

Let us now discuss two interacting cases rather than an isolated vortex. The first case we have in mind is a symmetrical vortex of one dot interacting with a single dipole moment located outside the dot, while the second case corresponds to the interaction of two symmetrical vortices, each associated with its own dot.

The interacting energy $E_{\mathbf{Gp}}$ for the first case can be evaluated as a dot product between the field produced by the vortex and the dipole moment **p** located at some distance from the dot. In other words,

$$E_{\mathbf{Gp}} = -\mathbf{E}^{(3)} \cdot \mathbf{p}, \tag{11}$$

where $\mathbf{E}^{(3)}$ is given by Eqs. (9) and (10). Equation (10) indicates that this interaction energy decreases with the distance as $1/R^6$, since **p** does not depend on the distance.

The interaction energy between two vortices, $E_{\mathbf{GG}}$, centered at two different dots, can be extracted from the Appendix:

$$E_{\mathbf{GG}} = -\frac{9\varepsilon_3}{4\pi\varepsilon_0(\varepsilon_1 + 2\varepsilon_3)(\varepsilon_2 + 2\varepsilon_3)}$$
$$\times \sum_{ij} \frac{R_{ij}^2 (\mathbf{p}_i^{(1)} \mathbf{p}_j^{(2)}) - 3(\mathbf{p}_i^{(1)} \mathbf{R}_{ij})(\mathbf{p}_j^{(2)} \mathbf{R}_{ij})}{R_{ij}^5}, \tag{12}$$

where $\mathbf{r}_i^{(1)}$ (respectively, $\mathbf{r}_j^{(2)}$) locates the site i (respectively, j) of the first (respectively, second) dot with respect to the center of the first (respectively, second) dot. $\mathbf{p}_i^{(1)}$ and $\mathbf{p}_j^{(2)}$ are the dipole moments at these sites i and j, respectively. $\mathbf{R}_{ij} = \mathbf{R} - \mathbf{r}_i^{(1)} + \mathbf{r}_j^{(2)}$, where **R** is the vector joining the centers of the two dots. Finally, ε_1, ε_2, and ε_3 are the high-frequency (electronic) dielectric constants in the first and second dots and in the intermediate region, respectively (see Appendix).

We numerically use the expression given by Eq. (12) as well as obtain an analytical expression for this interaction energy [by performing a multipole expansion of Eq. (12) with respect to $\mathbf{r}_i^{(1)}$ and $\mathbf{r}_j^{(2)}$] to determine three interesting energetic features of two interacting vortices. Such features are shown in Fig. 13 and are as follows: (1) their interaction energies decrease with the distance as $1/R^9$ (this is a rather weak interaction, which may be useful to avoid the cross-talking problem between two dots, i.e., one can imagine switching the chirality of the first vortex without modifying the chirality of the second vortex[2]); (2) the lowest interacting energy of two vortices corresponds to the case in which the toroidal moments of the two dots are parallel to each other and are aligned in a direction perpendicular to the **R** vector joining the center of the two dots; and (3) choosing $\mathbf{R} = \mathbf{z}$ (where **z** is the unit vector along the z axis) and forcing the toroidal moments of the two dots to be aligned either along z or $-z$ results, via the minimization of $E_{\mathbf{GG}}$, in the toroidal moments of these two vortices being antiparallel. These three features dramatically differ with the corresponding results for two interacting polarizations.

VII. CONCLUSIONS

In summary, we performed first-principles-based simulations to provide atomistic details of the dipole vortex struc-
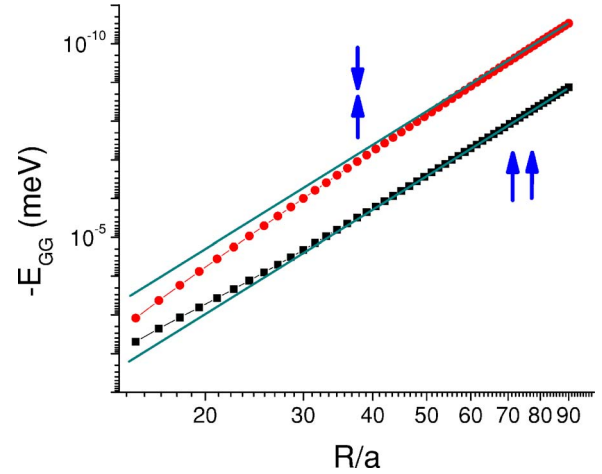

FIG. 13. (Color online) Dependency of the interaction energy between vortices centered at two different $12 \times 12 \times 12$ dots at 1 K on the distance (in units of the lattice constant of the five-atom unit cell), as obtained in our Monte Carlo computations. The straight lines show the fit by A/R^9 (where A is a constant). The lower curve corresponds to the ground state, for which the toroidal moments of the two dots are parallel to each other and are aligned in a direction perpendicular to the **R** vector joining the center of the two dots. The upper curve corresponds to the case for which the toroidal moments of the two dots are opposed to each other and face the other dot.

ture in ferroelectric nanodots, and its dependency on the dot's size and shape and on the material from which the dot is made of. These simulations, as well as analytical developments, also revealed the energy landscape associated with toroidal moments or striking features generated by the vortex structure. Examples of such features are (1) the peculiar spatial distribution of the inhomogeneous strain, (2) the axial ratio being lower than 1 if the formation of dipole vortex generates a tetragonal state, (3) the local electric field inside the dot exhibiting a vortex pattern, and (4) the electric field produced by a (symmetrical) dipole vortex outside the dot being described by a fourth-rank tensor and having peculiar signatures (such as a distance dependency of $1/R^6$ and oscillating in space when changing the polar angle for a fixed distance). Finally, we also determined and discussed the energetics of a vortex interacting with a dipole moment, and of two interacting vortices located in two different nanodots.

We hope that our discoveries (i) will help experimentalists in determining the vortex in ferroelectrics nanodots, (ii) will lead to a better understanding of (and stimulate further studies of) dipolar nanostructures, and (iii) will encourage scientists and engineers to use vortex properties in advanced nanoscale devices.

APPENDIX: INTERACTION BETWEEN DIPOLES LOCATED IN DIFFERENT POLARIZABLE SPHERES

Let us consider two polarizable spheres embedded in a polarizable media. We will denote ε_1 and ε_2 the high-frequency (electronic) dielectric constant of the first and second spheres, respectively, while ε_3 is the high-frequency (electronic) dielectric constant of the media. Let us further assume that there are dipole moments $\mathbf{d}^{(1)}$ and $\mathbf{d}^{(2)}$ in the first and second spheres, respectively. In the Onsager theory,[22] the field produced by the first sphere at a position $\mathbf{r}$, located in the intersphere region, is

$$\mathbf{E}_{media} = -\frac{1}{4\pi\varepsilon_0\varepsilon^*}\frac{r^2\mathbf{d}^{(1)} - 3(\mathbf{d}^{(1)}\mathbf{r})\mathbf{r}}{r^5}, \qquad (A1)$$

where ε_0 is the vacuum's permittivity, r is the length of $\mathbf{r}$, and $\varepsilon^* = (\varepsilon_1 + 2\varepsilon_3)/3$. Interestingly, Eq. (5) (which was the starting point to determine the field produced by a dipole vortex in the vacuum surrounding the dot) can be derived from Eq. (A1) when choosing a media made of vacuum, i.e., for which $\varepsilon_3 = 1$ and thus $\varepsilon^* = (\varepsilon_1 + 2)/3$.

Moreover, if the two spheres are far from each other, the field, $\mathbf{E}_{sphere2}$, produced by the $\mathbf{d}^{(1)}$ dipole of the first sphere

in the second sphere can be considered to be approximately uniform. In that case, the Onsager theory[22] gives the following expression:

$$\mathbf{E}_{sphere2} = -\frac{9\varepsilon_3}{4\pi\varepsilon_0(\varepsilon_1 + 2\varepsilon_3)(\varepsilon_2 + 2\varepsilon_3)}\frac{r^2\mathbf{d}^{(1)} - 3(\mathbf{d}^{(1)}\mathbf{r})\mathbf{r}}{r^5}, \qquad (A2)$$

and the interacting energy between the two dipoles located in the two spheres can be simply computed as the dot product between $-\mathbf{E}_{sphere2}$ and the dipole moment in this second sphere:

$$\begin{aligned} E_{dip} = &\frac{9\varepsilon_3}{4\pi\varepsilon_0(\varepsilon_1 + 2\varepsilon_3)(\varepsilon_2 + 2\varepsilon_3)} \\ &\times \frac{r^2(\mathbf{d}^{(1)}\cdot\mathbf{d}^{(2)}) - 3(\mathbf{d}^{(1)}\mathbf{r})(\mathbf{r}\cdot\mathbf{d}^{(2)})}{r^5}. \end{aligned} \qquad (A3)$$

Note that this expression coincides with the expression for the energy of the dipole-dipole interaction in a uniform media [that is, $\frac{1}{4\pi\varepsilon_0\varepsilon}\frac{r^2(\mathbf{d}^{(1)}\cdot\mathbf{d}^{(2)}) - 3(\mathbf{d}^{(1)}\mathbf{r})(\mathbf{r}\cdot\mathbf{d}^{(2)})}{r^5}$] when choosing $\varepsilon = \varepsilon_1 = \varepsilon_2 = \varepsilon_3$.

[1] H. Fu and L. Bellaiche, Phys. Rev. Lett. **91**, 257601 (2003).

[2] I. Naumov, L. Bellaiche, and H. Fu, Nature (London) **432**, 737 (2004).

[3] I. Ponomareva, I. I. Naumov, I. Kornev, Huaxiang Fu, and L. Bellaiche, Phys. Rev. B **72**, 140102(R) (2005); I. Ponomareva, I. I. Naumov, and L. Bellaiche, *ibid.* **72**, 214118 (2005).

[4] S. D. Bader, Rev. Mod. Phys. **78**, 1 (2006).

[5] A. Hubert and R. Schafer, *Magnetic Domains* (Springer, New York, 2000), pp. 167–168.

[6] M. Schneider, H. Hoffmann, and J. Zweck, Appl. Phys. Lett. **79**, 3113 (2001).

[7] S. Prosandeev, I. Ponomareva, I. Kornev, I. Naumov, and L. Bellaiche, Phys. Rev. Lett. **96**, 237601 (2006).

[8] W. Zhong, D. Vanderbilt, and K. M. Rabe, Phys. Rev. Lett. **73**, 1861 (1994); Phys. Rev. B **52**, 6301 (1995).

[9] L. Bellaiche, A. García, and D. Vanderbilt, Phys. Rev. Lett. **84**, 5427 (2000); Ferroelectrics **266**, 41 (2002).

[10] J. Iniguez and D. Vanderbilt, Phys. Rev. Lett. **89**, 115503 (2002).

[11] E. Almahmoud, Y. Navtsenya, I. Kornev, H. Fu, and L. Bellaiche, Phys. Rev. B **70**, 220102(R) (2004).

[12] I. I. Naumov and H. Fu, cond-mat/0505497 (unpublished).

[13] K. Nakamura, T. Ito, and A. J. Freeman, Phys. Rev. B **68**, 180404(R) (2003).

[14] B. Jaffe, W. R. Cook, and H. Jaffe, *Piezoelectric Ceramics* (Academic, London, 1971), p. 136.

[15] C. Kittel, Phys. Rev. **70**, 965 (1946).

[16] S. Prosandeev and L. Bellaiche, Phys. Rev. Lett. **97**, 167601 (2006).

[17] A. H. Kahn and J. Layendeccker, Phys. Rev. **135**, A1321 (1964).

[18] S. Tikadzumi, *Physics of Ferromagnetism: Magnetic Characteristics and Practical Applications* (Mir, Moscow, 1987).

[19] S. P. Li, D. Peyrade, M. Natali, A. Lebib, Y. Chen, U. Ebels, L. D. Buda, and K. Ounadjela, Phys. Rev. Lett. **86**, 1102 (2001).

[20] V. M. Dubovik and V. V. Tugushev, Phys. Rep. **187**, 145 (1990).

[21] Yu. I. Sirotin and M. P. Shaskolskaya, *The Principles of Crystal Physics* (Nauka, Moscow, 1979).

[22] L. Onsager, J. Am. Chem. Soc. **58**, 1486 (1936).